

RESEARCH ARTICLE

10.1002/2016JE005220

Key Points:

- Different impact characteristics of samples related by micrometeorite bombardment are studied through pulsed laser irradiation experiments
- Characteristics of subsurface structure and inclusion are related to rock type and mineral composition
- The structure and inclusion of lunar soil grain will help determine the source of npFe and infer the types of micrometeorite impactors

Supporting Information:

- Supporting Information S1

Correspondence to:

X. Li and W. Yao,
lixiongyao@vip.skgg.cn;
yaowq@tsinghua.edu.cn

Citation:

Wu, Y., Li, X., Yao, W., & Wang, S. (2017). Impact characteristics of different rocks in a pulsed laser irradiation experiment: Simulation of micrometeorite bombardment on the Moon. *Journal of Geophysical Research: Planets*, 122, 1956–1967. <https://doi.org/10.1002/2016JE005220>


Received 18 NOV 2016

Accepted 31 AUG 2017

Accepted article online 5 SEP 2017

Published online 9 OCT 2017

Impact Characteristics of Different Rocks in a Pulsed Laser Irradiation Experiment: Simulation of Micrometeorite Bombardment on the Moon

Yanxue Wu^{1,2,3} , Xiongyao Li¹, Wenqing Yao³, and Shijie Wang¹

¹Center for Lunar and Planetary Sciences, Institute of Geochemistry, Chinese Academy of Sciences, Guiyang, China, ²College of Earth Science, University of Chinese Academy of Sciences, Beijing, China, ³Department of Chemistry, Tsinghua University, Beijing, China

Abstract Without the protection of the atmosphere, the soils on lunar surfaces undergo a series of optical, physical, and chemical changes during micrometeorite bombardment. To simulate the micrometeorite bombardment process and analyze the impact characteristics, four types of rocks, including terrestrial basalt and anorthosite supposed to represent lunar rock, an H-type chondrite (the Huaxi ordinary chondrite), and an iron meteorite (the Gebel Kamil iron meteorite) supposed to represent micrometeorite impactors, are irradiated by a nanosecond pulse laser in a high vacuum chamber. Based on laser irradiation experiments, the laser pits are found to be of different shapes and sizes which vary with the rock type. Many melt and vapor deposits are found on the mineral surfaces of all the samples, and nanophase iron (npFe) or Fe-Ni alloy particles are typically distributed on the surfaces of ilmenite, kamacite, or other minerals near kamacite. By analyzing the focused ion beam ultrathin slices of laser pits with a transmission electron microscope, the results show that the subsurface structures can be divided into three classes and that npFe can be easily found in Fe-bearing minerals. These differences in impact characteristics will help determine the source material of npFe and infer the type of micrometeorite impactors. During micrometeorite bombardment, in the mare regions, the npFe are probably produced simultaneously from lunar basalt and micrometeorites with iron-rich minerals, while the npFe in the highlands regions mainly come from micrometeorites.

Plain Language Summary Micrometeorite bombardment of the surfaces of planetary bodies without the protection of atmosphere is a common phenomenon that changes the physical and chemical properties of soils exposed on the airless lunar surface. To understand the micrometeorite bombardment process and analyze systematically the impact characteristics, we designed a pulsed laser irradiation experiment which could simulate the micrometeorite bombardment. The results show that the subsurface structures of minerals irradiated by a pulsed laser can be divided into three classes and that nanophase iron inclusions can be easily found in Fe-bearing minerals. Characteristics of subsurface structure and inclusions are related to rock type and mineral composition. So these differences in impact characteristics will help determine the source material of nanophase iron and infer the type of micrometeorite impactors. During micrometeorite bombardment, in the mare regions, nanophase iron are probably produced simultaneously from lunar basalt and micrometeorites with iron-rich minerals, while the nanophase iron in the highland regions mainly come from micrometeorites.

1. Introduction

Micrometeorite bombardment is one of the most important processes of space weathering on the Moon (Hapke, 2001; Pieters & Noble, 2016). Without the protection of the atmosphere, the Moon has suffered serious micrometeorite bombardment since it was formed 4.5 Gy ago, which has resulted in significant changes in chemistry, mineralogy, microstructure, and morphology of the surface material (Chapman, 2004; Clark et al., 2002; Dobrica & Oglione, 2016; Hapke, 2001; Keller & McKay, 1993, 1997). These studies of the micrometeorite bombardment process and its consequences will improve understanding of the evolution of the lunar surface and lunar remote sensing data (Fassett & Minton, 2013).

Until recent years, the investigation of space weathering on the Moon was still mostly based on the samples returned from the Apollo missions and several lunar meteorites (Bernatowicz et al., 1994; Bibring et al., 1972; Hapke et al., 1975; Keller & McKay, 1993; Noble et al., 2005, 2010; Pieters et al., 2000; Taylor et al., 2001). It is widely accepted that the majority of space weathering effects in samples are caused by solar wind

implantation and micrometeorite bombardment (Fassett & Minton, 2013; Hapke, 2001; Pieters & Noble, 2016). For lunar soil grains, both of the processes can alter their chemistry, mineralogy, microstructure, and morphology, such as the production of nanophase Fe (npFe) and the formation of amorphous rims in the grain surface layers. The npFe can be produced as inclusions in the amorphous rims or the agglutinate glass through vapor deposition or melting (Keller & McKay, 1997; Thompson et al., 2016). The amorphous rims can be formed through crystal structure breakdown as a result of solar wind irradiation (Bradley, 1994; Keller & McKay, 1997; Li et al., 2013). They can also be formed through the recondensation of the target (lunar rocks) and impactor material (micrometeorites, themselves) on grain surfaces by micrometeorite bombardment. Differences in chemical composition can help to differentiate between solar wind irradiation and vapor deposited rims (Keller & McKay, 1997; Noguchi et al., 2014; Thompson et al., 2014). To investigate the effects of simulated micrometeorite bombardment on samples with different compositions, the impact characteristics of related rocks and impactors after micrometeorite bombardment need to be studied.

Laser irradiation experiments have been used widely in the community to simulate micrometeorite impact space weathering processes. Bombarding the samples with high-velocity particles is the most direct and effective method to simulate the micrometeorite bombardment, while high-velocity impact experiments at a speed of more than 10 km/s could hardly produce enough number of dust impacts (Yamada et al., 1999). The use of a pulsed laser to simulate the micrometeorite bombardment was reported in the 1990s. Moroz et al. (1996) and Wasson et al. (1998) irradiated ordinary chondrites, olivine grains, clinopyroxene grains, olivine-clinopyroxene mixture, and HED meteorites with microsecond pulse lasers to study their spectral changes. To better simulate the impact timescale, Sasaki et al. (2001, 2002) used a nanosecond pulse laser to simulate the micrometeorite bombardment processes. In Sasaki's experiment, olivine grains and pyroxene grains were irradiated by a pulsed laser beam with a wavelength of 1,064 nm under a vacuum of $(1-2) \times 10^{-5}$ torr. The pulse duration was 6–8 ns, which reached the timescale of micrometeorite bombardment (Yamada et al., 1999). In the irradiated samples from Sasaki et al. (2001) npFe grains were observed, and spectral changes were obvious after pulsed laser irradiation. Then, Brunetto et al. (2006) simulated the effects of micrometeorite bombardment on minor bodies of the solar system using a nanosecond pulse UV excimer laser at two different wavelengths, 193 and 248 nm. In addition, Loeffler et al. (2008) simulated the micrometeorite bombardment process using a pulsed laser at ultrahigh vacuum (UHV) and discussed the effect of redeposition of impact ejecta on the spectral properties. In previous studies, the simulation of micrometeorite bombardment is mainly focused on the discussion of spectral changes (Matsuoka et al., 2015; Noble et al., 2011).

Coupling spectral analyses and microstructural characterization is a powerful way to understand the effects of micrometeorite bombardment (Gillis-Davis et al., 2017; Loeffler et al., 2016). But the impact characteristics of different rocks are not analyzed systematically and related to the micrometeorite bombardment process. In this study, four types of samples are irradiated by a nanosecond pulse laser in a UHV chamber, and their impact characteristics are analyzed.

2. Experiment

2.1. Experimental Configuration

The base pressure of the ion-pumped high vacuum chamber for the laser irradiation experiments is greater than 5×10^{-6} Pa, and the high vacuum chamber is a part of the UHV surface analysis system located in the Center for Lunar and Planetary Sciences, Institute of Geochemistry, Chinese Academy of Sciences. A 6 ns pulsed laser at a wavelength of 532 nm from a YAG laser was used to irradiate the target 10 times at a fixed point with a laser frequency of 1 Hz. Before the laser beam irradiated the targets, it passed through a fused-silica window, which was measured to have 90% transmittance at 532 nm. The laser beam, with a diameter of 500 μm , struck the target vertically with an energy per pulse of 200 mJ. In this case, the energy density that strikes the target reaches 10^3 mJ/mm², and the power density is above 10^{10} W/cm² where there are melting, evaporation, and ion formation processes (Kissel & Krueger, 1987; Yamada et al., 1999).

After irradiation, the chamber was opened, and the samples were analyzed using a focused ion beam scanning electron microscope (FIB-SEM) and a transmission electron microscope (TEM). The SEM and energy-dispersive X-ray spectrometer (EDS) mounted in the SEM were used to measure the morphology and

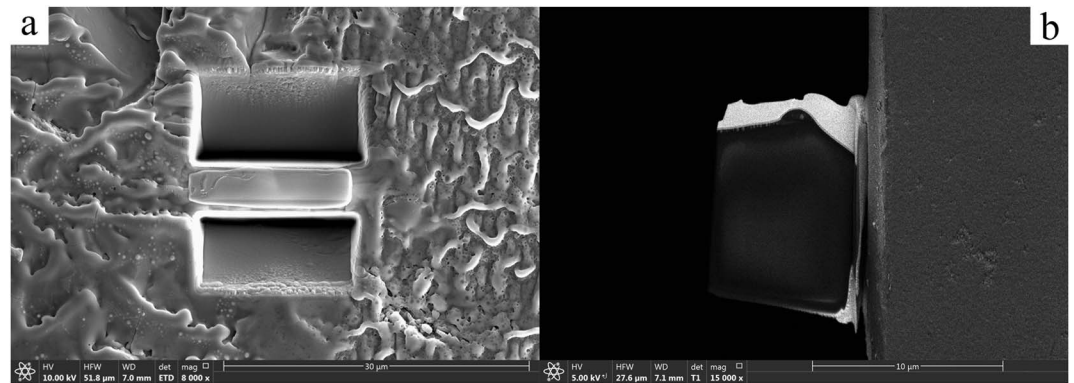


Figure 1. (a) Secondary electron (SE) image of the location of the FIB slice in the basalt bombarded by pulsed laser. (b) Backscattered electron (BSE) image of FIB ultrathin slice.

composition of the samples, respectively. To observe the microstructure of the subsurface layer of samples with the TEM, the FIB-SEM system was used to prepare slices (Figures 1a and 1b).

2.2. Samples

Basalt and anorthosite are the two main rock types on the Moon. They are distributed in the lunar mare and lunar highlands, respectively. To determine the impact characteristics of lunar rock, terrestrial basalt and anorthosite are chosen to be the first two samples in the experiment. In addition, the Huaxi ordinary chondrite and the Gebel Kamil iron meteorite are also chosen to represent stony micrometeorite and iron micrometeorite, respectively. All the samples were polished with 10,000 mesh diamond micropowder before being irradiated with the pulsed laser.

3. Results and Analysis

3.1. Laser Pits

After irradiation by the pulsed laser, the laser pits in these rocks show different shapes and sizes (Figure 2). With the 500 μm spot size of the laser beam irradiation, the laser pits sizes range from 0.5 mm to more than 1 mm. Relative to the round shape of the laser pits in anorthosite and the Gebel Kamil iron meteorite (Figures 2b and 2d), those in basalt and Huaxi ordinary chondrite are irregular (Figures 2a and 2c). Anorthosite and the Gebel Kamil iron meteorite show round-shaped pits for their single mineral composition. However, the depths and surface roughness of laser pits are considerably different between these two rocks. Basalt and Huaxi ordinary chondrite, which have complex mineral compositions, both show irregular pit shapes. For basalt and Huaxi ordinary chondrite, plagioclase, pyroxene, and olivine have rough surface morphologies (Figures 3a–3c). In Figure 3b, the ilmenite in basalt surface is still flat and contains cracks and small holes. However, the kamacite in Huaxi ordinary chondrite displays ripples on a flat surface, which is similar to the surface morphology of the pit in the Gebel Kamil iron meteorite (Figures 3c and 3d).

3.2. Melt and Vapor Deposits

The melt and vapor deposits are produced in the irradiation process by the melting and vaporization of the surface of the irradiation targets. A large quantity of melt and vapor deposits is found on the mineral surface in each sample. Most of the melt and vapor deposits are spherical with diameters ranging from several nanometers to hundreds of nanometers (Figure 4). However, there are certain differences in their chemical compositions. For basalt, EDS analyses indicate that the melt and vapor deposits on the surfaces of olivine, pyroxene, and plagioclase are mainly silicates and aluminosilicates (Figure 4a). The melt and vapor deposits are mainly npFe particles on the surface of ilmenite (Figure 4b). For anorthosite, the melt and vapor deposits are relatively simple, and their chemical composition is primarily aluminosilicate. Silicate and aluminosilicate spherical particles are mainly distributed on the surfaces of olivine, pyroxene, and plagioclase in Huaxi ordinary chondrites, which are the same as in basalt. On the surface of kamacite, the melt and vapor deposits are mainly npFe or Fe-Ni alloys, which are similar to those in the Gebel Kamil iron meteorite. Near the kamacite, there are also some npFe or Fe-Ni alloy particles on the surfaces of olivine and pyroxene. These nanophase

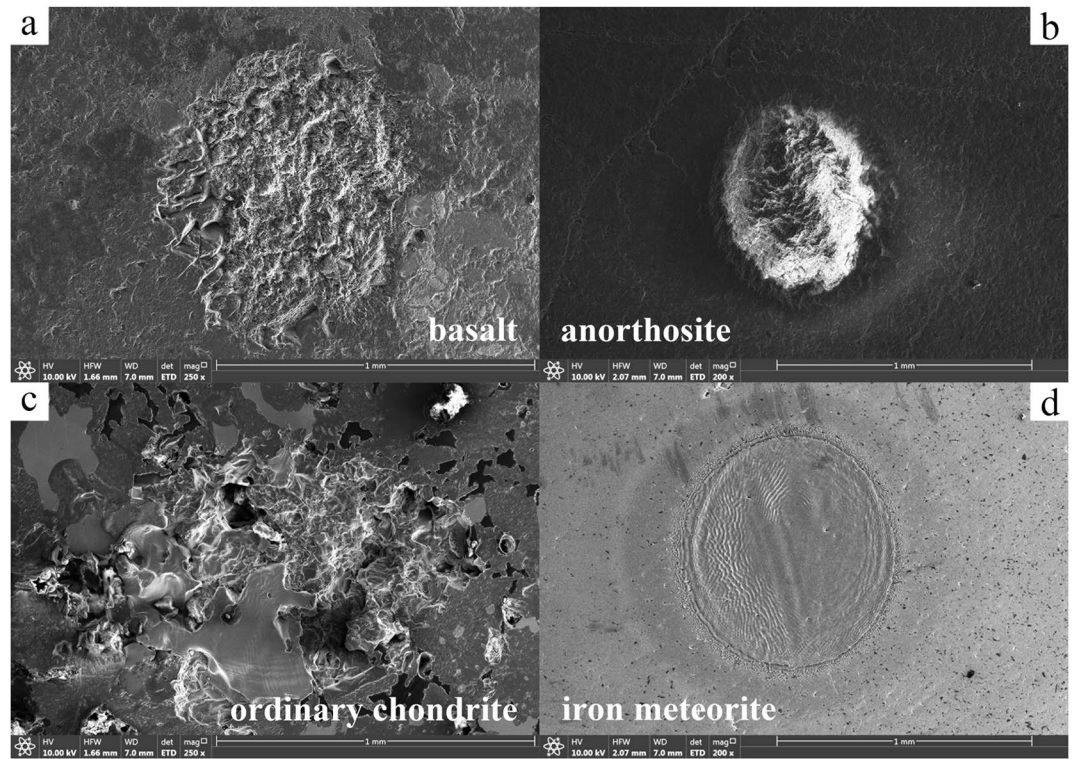


Figure 2. SE images of the laser pits of different rocks, produced by pulsed laser bombardment. (a) Basalt. (b) Anorthosite. (c) Huaxi ordinary chondrite. (d) Gebel Kamil iron meteorite.

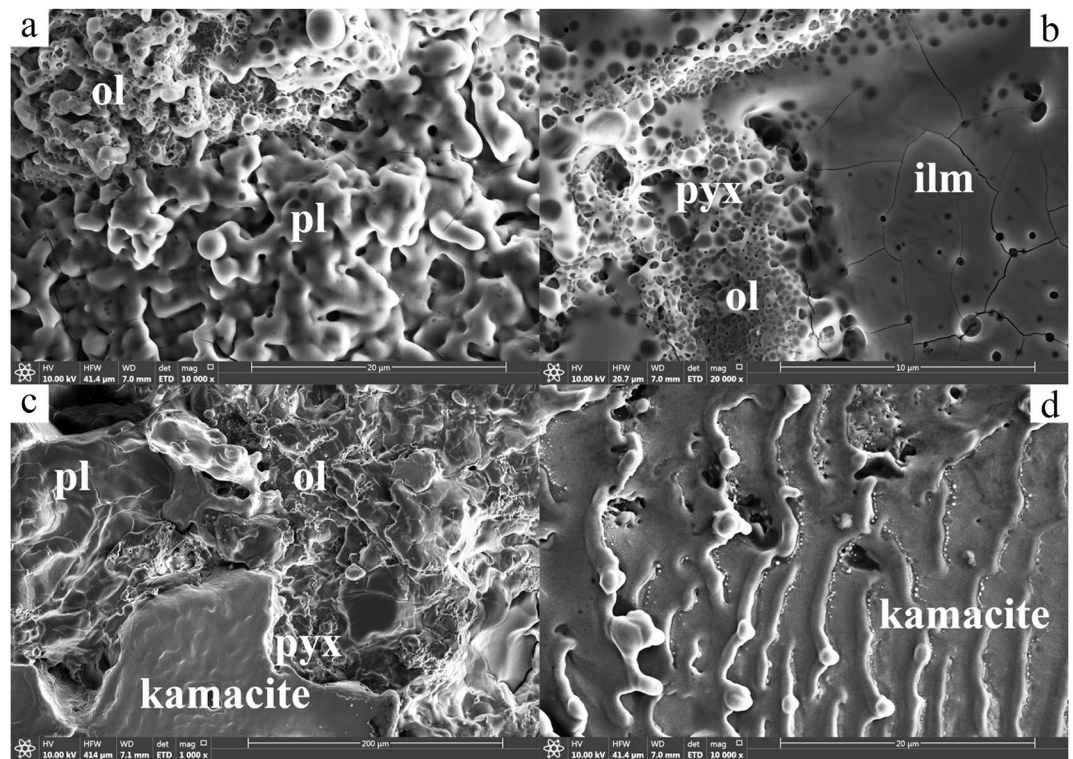


Figure 3. SE images of surface morphologies of different minerals after being bombarded by a pulsed laser. (a, b) Images of the pit of basalt. (c, d) Images of the pits of Huaxi ordinary chondrite and the Gebel Kamil iron meteorite, respectively. In the images, ol is olivine, pl is plagioclase, ilm is ilmenite, and pyx is pyroxene.

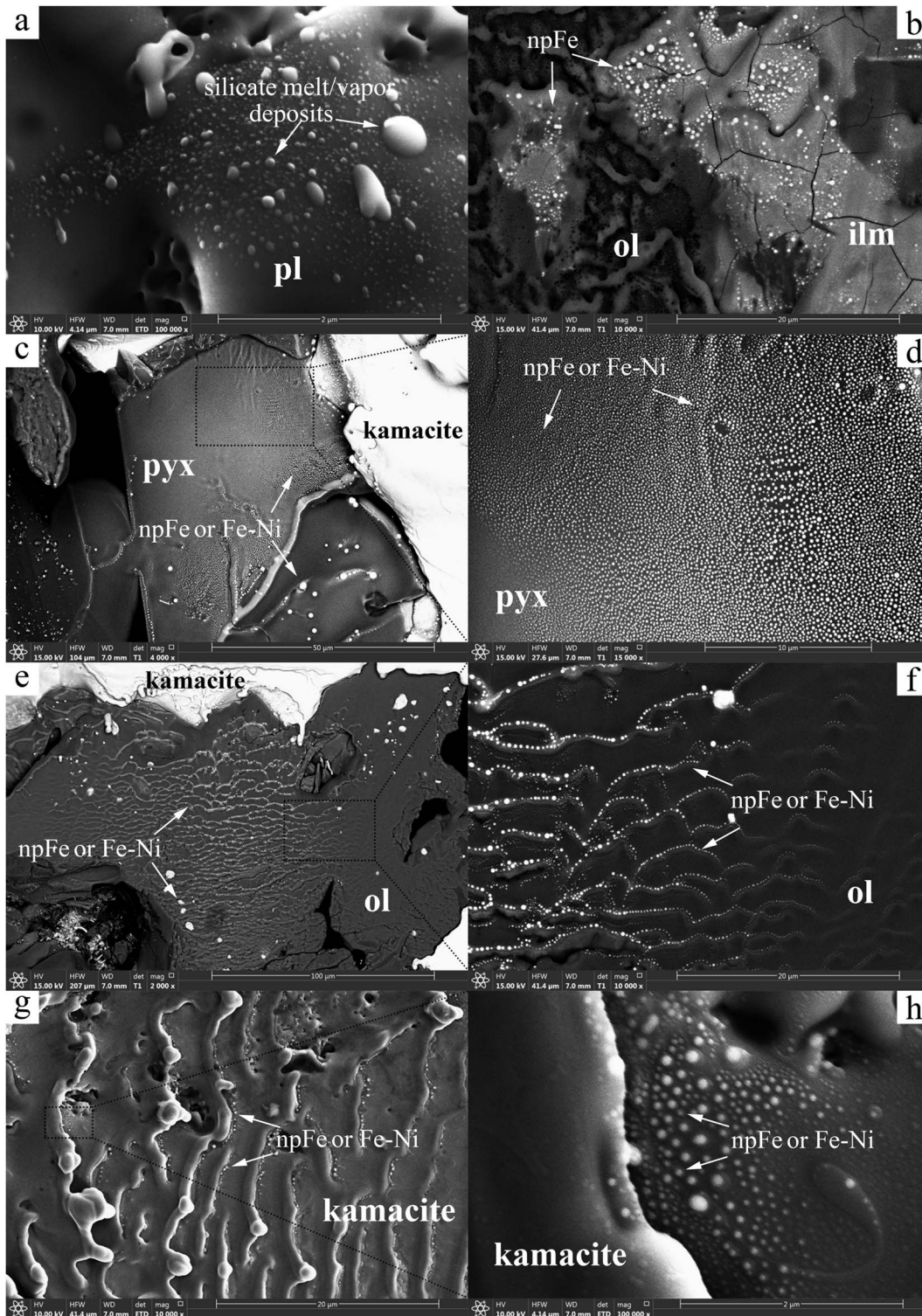


Figure 4. (a) SE image of silicate and aluminosilicate particles on the silicate mineral surface in basalt. (b) BSE image of npFe on the ilmenite surface in basalt. (c) BSE image of nanophase metal particles on the surface of pyroxene near to kamacite (white region on the left) in Huaxi ordinary chondrite. (d) BSE image of uniform distribution of nanophase metal particles in Figure 4c. (e) BSE image of nanophase metal particles on the surface of olivine near kamacite (white region on the top) in Huaxi ordinary chondrite. (f) BSE image of nanophase metal particles concentrated at the edges of ripple-shaped ridges in Figure 4d. (g) SE image of ripple-shaped ridges and nanophase metal particles on kamacite surface in Gebel Kamil iron meteorite. (h) SE image of nanophase metal particles distributed at the edges of ripple-shaped ridges in Figure 4g.

metal particles are distributed uniformly on the surface of pyroxene, and their particle sizes tend to decrease from the nearside kamacite to the farside (Figures 4c and 4d). On the contrary, the nanophase metal particles are distributed nonuniformly on the surface of the olivine. They are concentrated at the edges of ripple-shaped ridges (Figures 4e and 4f) which is consistent with Loeffler et al. (2016) studies. For the Gebel Kamil iron meteorite, the characteristics of melt and vapor deposits are similar to those of kamacite in Huaxi ordinary chondrite (Figures 4g and 4h).

3.3. TEM Analysis of the Irradiated Samples

To analyze the subsurface structures of the laser pits, we extracted thin sections with the FIB for analysis in the TEM. The results show that the subsurface structures can be divided into three classes. The first is a three-layer structure: a completely amorphous layer embedded with a few npFe particles in which there is a diffraction characteristic of complete amorphization, a partially amorphous layer embedded with many npFe particles in which there is a diffraction characteristic of polycrystalline ring pattern, and the irradiated target. The second class is a four-layer structure, in which there is an extra vapor-deposited layer on the outermost surface compared to the first class. The last is a two-layer structure in which only an amorphous layer covers the irradiated target.

All the subsurface structures of the four main minerals in basalt are three-layer structures (Figure 5). The amorphous layers are 100–200 nm in total thickness. For comparison of these different amorphous layers of the four minerals, the characteristics of inclusions are shown to distinguish the differences. In olivine, many inclusions are found in each of the two amorphous layers (Figure 5a), and their sizes range from several nanometers to 10 nm. With high-resolution transmission electron microscopy (HRTEM), the interplanar spacing of the inclusions is measured in the high-resolution image as 0.204 nm (Figures 5b and 5c). This value is consistent with the interplanar spacing of (101) in α -Fe of 0.203 nm (Thompson et al., 2015).

In pyroxene (Figure 5d), the inclusions are identified with high-resolution images according to their interplanar spacing (Figures 5e and 5f). The results show that the inclusions are mainly npFe. The content of npFe is relatively lower than that in olivine, which is compatible with Yamada et al. (1999) studies, and the diameters of npFe are usually less than 10 nm. These npFe are mainly concentrated in the partially amorphous layer, and a small amount of them are distributed in the completely amorphous layer.

Although the three-layer structure is also formed in plagioclase, there is no npFe in the amorphous layers for there is not an iron element in plagioclase (Figure 5g). In ilmenite (Figure 5h), npFe are also identified by their interplanar spacing (Figure 5i), and they are distributed almost exclusively in the partially amorphous layer, whose maximum size can reach 200 nm (Figure 5h). Some of them are sufficiently large to break through the completely amorphous layer and expose on the outer surface.

The subsurface structures of minerals in Huaxi ordinary chondrite can be classified into four-layer and two-layer structures. The subsurface structure of kamacite exhibits a two-layer structure in which an amorphous layer overlays the substrate (Figure 6a). Although many inclusions are also found in the amorphous layer, their distribution is different from that in basalt. Those of silicate minerals which are dozens of microns away from kamacite usually have a four-layer structure (Figures 6b and 6c), in which many npFe, identified by the interplanar spacing, are observed in the outer three layers (Figures 6d and 6e). However, silicate minerals near kamacite show a two-layer structure in which a vapor-deposited layer covers the substrate (Figure 6f) which is consistent with Loeffler et al. (2016) studies. In this layer, npFe of several nanometers to hundreds of nanometers are also identified by their interplanar spacing (Figures 6g and 6h). The amorphous layer in the four-layer structure of silicate minerals has the same characteristics as those in basalt. The total thickness of the amorphous layer is 150 nm, and many npFe several nanometers in size are embedded in the amorphous layer. The formation mechanism of these layers is similar to that in basalt.

Outside the interface, there is a region without any inclusion, and npFe or Fe-Ni are concentrated in the top-most layer, which is different from the irradiated target in chemical composition by EDS analyses and shows detectable vapor characteristics. The subsurface structures of olivine far from and near kamacite in Huaxi ordinary chondrite are shown in Figures 6c and 6f, respectively. Each of them has a clear interface between the vapor-deposited layer and the underlying layers. Relative to the olivine far from kamacite, the subsurface structures of those near kamacite in Huaxi ordinary chondrite exhibit a two-layer structure rather than amorphous layers (Figure 6f).

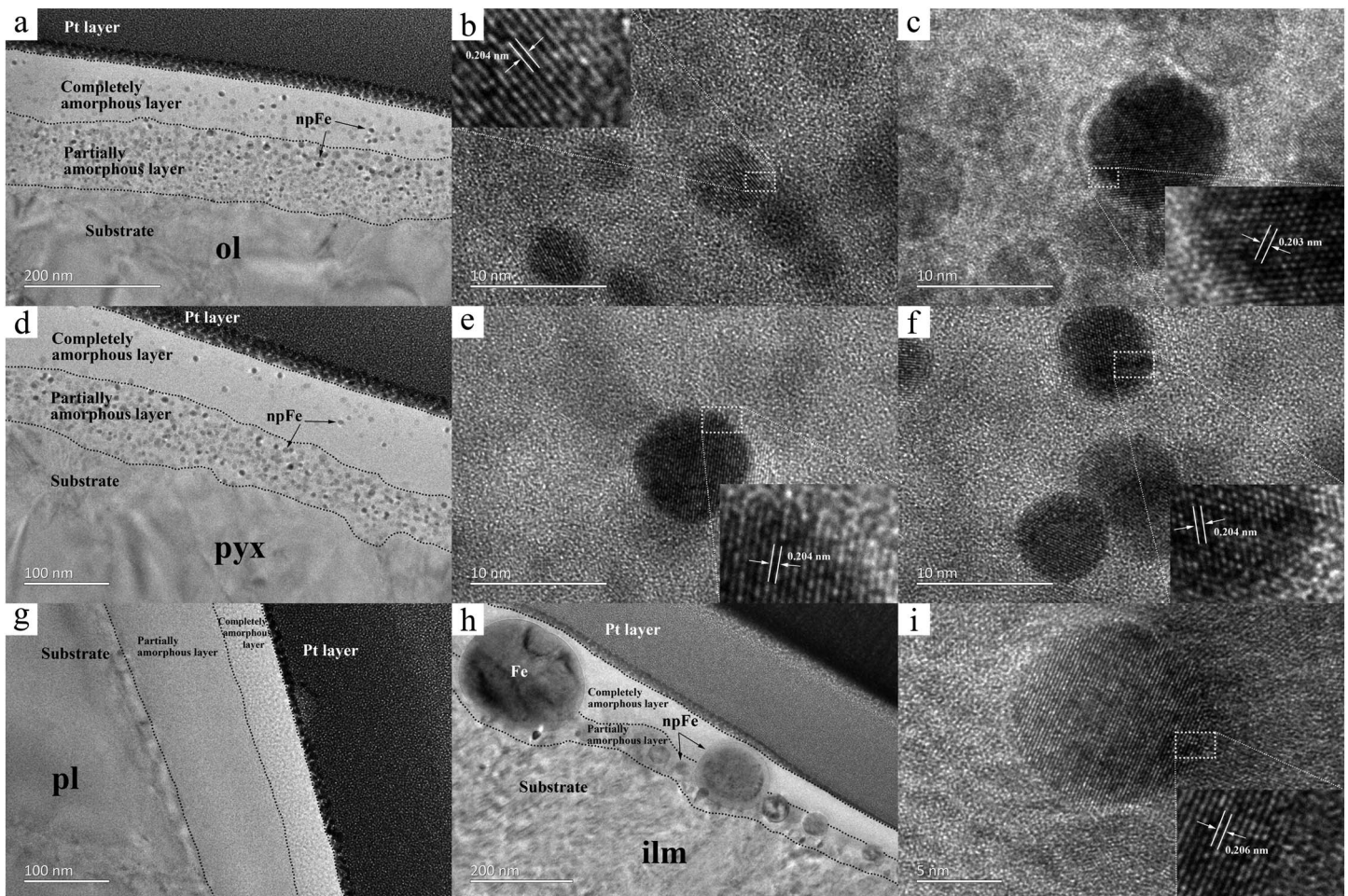


Figure 5. TEM and HRTEM images of minerals in basalt by pulsed laser bombardment. (a) Three-layer structure of olivine; black and gray round spots in amorphous layers are npFe. (b) npFe in a completely amorphous layer of Figure 5a. (c) npFe in a partially amorphous layer of Figure 5a. (d) Three-layer structure of pyroxene. (e) npFe in a completely amorphous layer of Figure 5d. (f) npFe in a partially amorphous layer of Figure 5d. (g) HRTEM images of plagioclase in basalt bombarded by pulsed laser. It also shows a three-layer structure, but there is no inclusion in the amorphous layers. (h) Three-layer structure of ilmenite. Some of the npFe are large enough to break through the completely amorphous layer and be exposed on the outer surface. There is no inclusion in the completely amorphous layer. (i) npFe in the completely amorphous layer. The high-resolution TEM images show that the interplanar spacing of the inclusions is 0.203–0.206 nm, which is consistent with the interplanar spacing of (101) in α -Fe of 0.203 nm.

For the interplanar spacing of (101) in α -(Fe, Ni) is also 0.203 nm, it is difficult to distinguish between α -Fe and α -(Fe, Ni) only through their interplanar spacing. To verify the source of those inclusions in Huaxi ordinary chondrite, their chemical composition is mapped by EDS embedded in the TEM (Figure 7). Due to the spatial resolution limitation of EDS, only two larger inclusions in the slice cut from pyroxene near kamacite are analyzed. The large inclusions have relative high Ni content in addition to Fe (Figures 7b and 7c). The Ni contents of inclusions A and B are 3.3 at. % and 1.7 at. %, respectively. This finding indicates that the inclusions come from kamacite because the pyroxene contains little Ni and the kamacite contains a large amount of Ni.

4. Discussion

Compared with the pyroxene and olivine in Huaxi ordinary chondrites, there are few npFe particles on the surfaces of pyroxene and olivine in basalt. In addition, those npFe particles distributed on the surfaces of pyroxene and olivine that originate from kamacite by vaporization. This mechanism is confirmed by the high content of Ni in these nanophase metal particles and extremely low content of Ni in the substrate. Furthermore, the presence of few npFe particles on the surfaces of pyroxene and olivine in basalt and

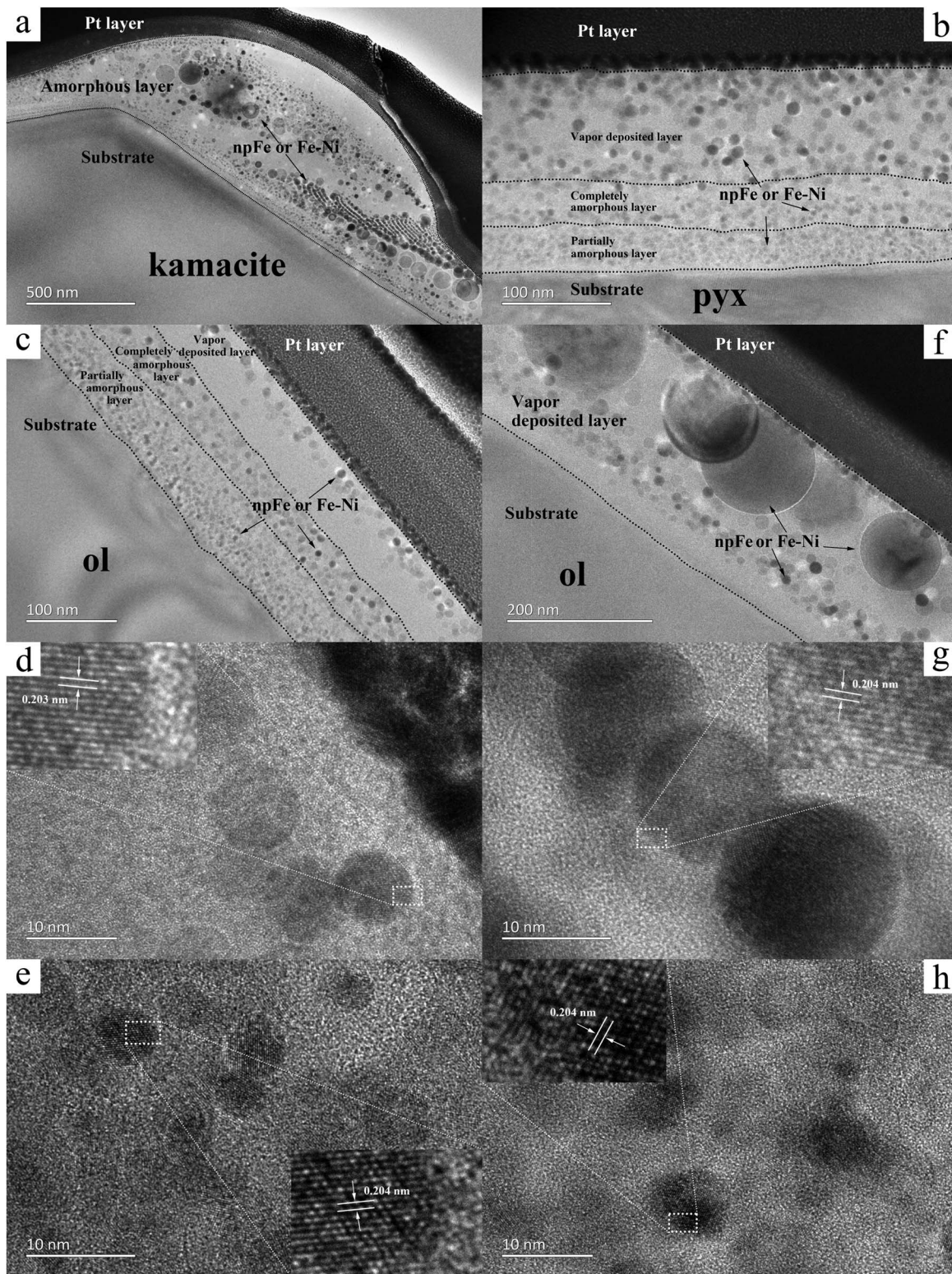


Figure 6. TEM and HRTEM images of minerals in Huaxi ordinary chondrites by pulsed laser bombardment. (a) Two-layer structure of kamacite. (b, c) Four-layer structure of pyroxene and olivine far from kamacite, respectively. (d, e) npFe in the amorphous layer and vapor-deposited layer in Figure 6c, respectively. The top left high-resolution image in Figure 6d and bottom right high-resolution image in Figure 6e show that the interplanar spacing of the inclusion is 0.203 nm and 0.204 nm, respectively. (f) Two-layer structure of olivine near to kamacite. (g, h) npFe in the amorphous layer and vapor-deposited layer in Figure 6f, respectively. The top right high-resolution image in Figure 6g and top left high-resolution image in Figure 6h show that both of the interplanar spacing of the two inclusions are 0.204 nm. This is consistent with the interplanar spacing of (101) in α -Fe, which is 0.203 nm. Black and gray round spots in Figures 6a–6h are npFe or Fe-Ni.

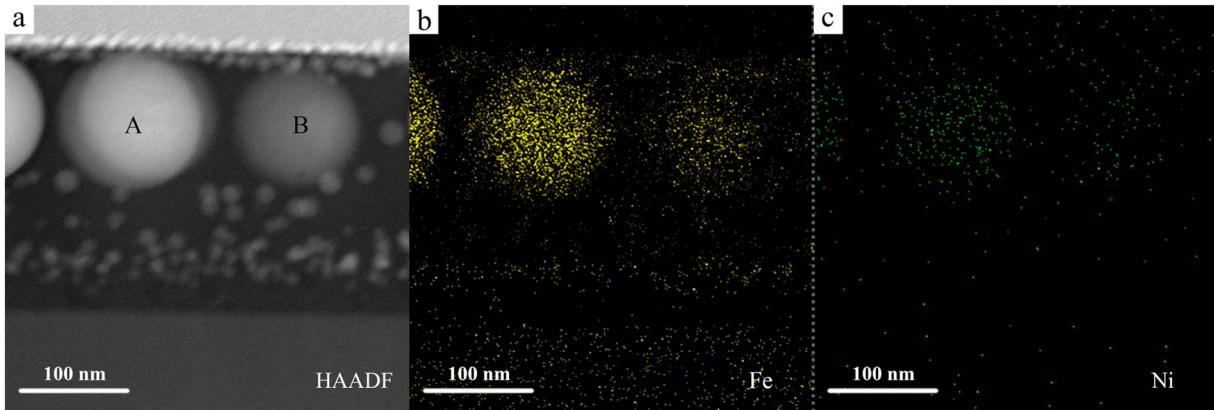


Figure 7. EDS mapping images of pyroxene near kamacite in Huaxi ordinary chondrite by pulsed laser bombardment. The large inclusions have relative high Ni content.

many in Huaxi ordinary chondrite also indicates that ilmenite is more difficult to vaporize than kamacite. The reason may be that the metal bond in kamacite is weaker than the ionic bond in ilmenite.

In our work, the obvious difference with previous studies such as Christoffersen et al. (2016) is that the amorphous layer is divided into partially amorphous layer and completely amorphous layer which is similar to Loeffler et al. (2016) studies. And the vapor-deposited layer only can be easily observed in some places, such as the olivine and pyroxene near kamacite, and this layer, when present, is enriched in npFe or Fe-Ni (Figure 8a), which is similar to Noble et al. (2011, 2016) studies (Figure 8b).

The three-layer structure is formed mainly from melting, subsequent quenching, and deposition of vapor. Due to the remarkable difference in the propagation speed in the interface between the mineral surface and the vacuum, most of the laser energy is converted to heat energy, which heats the mineral surface first. The surface materials of a mineral are melted when the temperature is higher than their melting point. Then, the subsurface materials are heated by heat conduction. Due to the loss of heat energy in

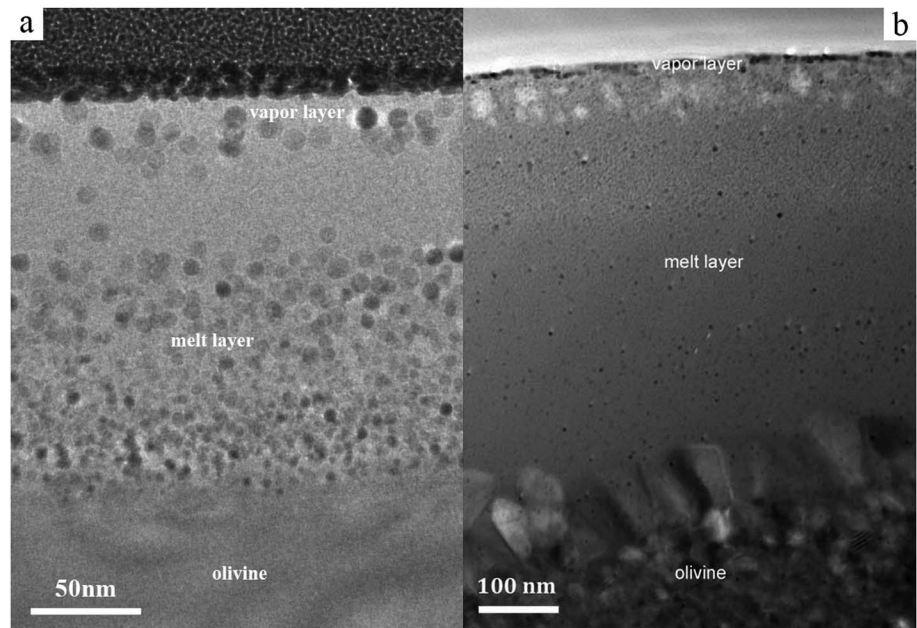


Figure 8. (a) TEM image of the subsurface structure in olivine far from kamacite by pulsed laser bombardment, which shows that npFe or Fe-Ni is produced in the melt and vapor layer. (b) TEM image of the subsurface structure in olivine by natural micrometeoroid impacts (Noble et al., 2016).

Table 1
Melting Points and Densities of Main Minerals

Main mineral	Melting point (°C)	Density (g/cm ³)
Olivine	1,250–1,890	3.27–4.37
Pyroxene	900–1,000	3.22–3.56
Plagioclase	1,215–1,550	2.61–2.76
Ilmenite	1,050	4.30–4.60
Kamacite	800–900	7.90

Note. The data in Table 1 are freely available at <https://www.americanelements.com/>.

conduction, the temperature decreases from the mineral surface to the interior. Therefore, it could be observed in the three-layer structure that the outermost layer is melted completely and quenched to glass and that the layer near the substrate is only partially melted. The completely amorphous layers in pyroxene and ilmenite are much thicker when compared to the layers observed in olivine and plagioclase. This may be a result of higher melting points for olivine and plagioclase than those for pyroxene and ilmenite (Table 1). This order results in deeper complete melting of the subsurface material and the formation of a relatively thicker completely amorphous layer.

Comparing the content of npFe, the higher content in the partially amorphous layer indicates that npFe is crystallized from the partial melt, which has a small temperature gradient. With a small temperature gradient, npFe has enough time to nucleate and form nanoparticles from the partial melt, which is covered by the outermost complete melt and cools down more slowly. In contrast, the outermost complete melt is directly exposed to the vacuum and cools down too fast.

In addition to the temperature gradient, crystallization of npFe is also affected by the Fe content of the melt. The higher the Fe content, the more npFe is crystallized. In the basalt, the olivine melt has the higher Fe content, and the Fe content is low in the plagioclase melt. Thus, there are more npFe in olivine and fewer of them in plagioclase. However, it is not well understood why the ilmenite has relatively fewer npFe even though it has the highest Fe content. The reason might be that the melting point of ilmenite is lower, which leads to a longer crystallization time and the development of some npFe by combining many nearby small inclusions in this period. Therefore, some large npFe are found in the amorphous layer, and it just appears that there are fewer npFe in the partially amorphous layer. If npFe grains are large enough, they protrude above the outer surface, which is consistent with Christoffersen et al. (1994, 1996) studies.

With the action of the shock wave, the melt with npFe is pushed outward, forming the ripple shape on the surface of kamacite. In this process, the heavier npFe are left beneath the ridge of the ripple, and some of them develop larger by combining many nearby small npFe.

For olivine near the kamacite, their surface is covered instantaneously with melt and vapor deposits from kamacite; the heat effect of the pulsed laser occurs on these melt and vapor deposits, and there is little thermal modification on the olivine surface that is near the kamacite. The heavier npFe condense lasts on the olivine surface. For olivine far from kamacite, only the small particles can travel such a long distance. Therefore, smaller and more concentrated npFe are observed in Figure 6c. In contrast, inclusions in the subsurface of olivine near kamacite are distributed in a thicker layer, and some of them develop larger by gathering small inclusions nearby (Figure 6f).

In the lunar mare regions, the concentration of npFe can reach 1.0 eq wt % (Morris, 1980), and basalt is the major rock, which consists of olivine, pyroxene, plagioclase, and ilmenite. Based on the pulsed laser bombardment experiment, large amounts of npFe can be produced in basalt. In olivine and pyroxene, npFe are distributed in the amorphous layers, and their sizes range from several nanometers to 10 nm. For ilmenite, the maximum size of npFe can reach 200 nm, and some of them develop sufficiently large to expose on the surface and are easily observed by SEM. Only in plagioclase is npFe not found. The findings presented here are consistent with previous experiments and show Fe-bearing minerals in basalt that are important source materials from which npFe is produced during the micrometeorite bombardment processes.

In natural micrometeoroid impacts, as impactors, most micrometeorites, including stony meteorite, iron meteorites, and stony-iron meteorites, which contain iron-rich minerals, such as olivine, pyroxene, troilite, and kamacite, are also some of the most important source materials to produce npFe. Particularly in kamacite, there are plenty of npFe melt and vapor deposits and npFe, whose sizes range from several nanometers to hundreds of nanometers, and the more prominent difference is that they contain small amounts of Ni relative to silicate minerals (Grant et al., 1973). Both lunar mare soils and micrometeorites can be the source of npFe. Therefore, in the mare regions, the npFe is produced simultaneously from lunar basalt and micrometeorites with iron-rich minerals during micrometeorite bombardment (Figures 8a and 8b).

In the lunar highlands regions, the concentration of npFe can reach 0.7 eq wt % (Morris, 1980), and the major rock is anorthosite, which consists of plagioclase or anorthite. The experiment suggests that the presence of npFe in the highlands regions could be a consequence of the micrometeorites themselves or minor phases with iron minerals in soils. In the lunar sample, many npFe had been found in the anorthite surface rim of 10,084, although the amorphous rim without npFe had been found in 78,221 (Keller & McKay, 1997; Noble et al., 2005). Thus, it can be inferred that the formation of npFe in the rim in 10084 is related to a micrometeorite bombardment process with an impactor enriched iron-rich minerals, such as iron meteorite, H ordinary chondrite, and E chondrite. The source of the npFe is the vaporization of kamacite in the impactor. This inference is consistent with previous studies that showed that such npFe rims form largely through the condensation of impact-generated vapors deposition since their compositions are distinct from those of the host grains and are a depositional feature of lunar grains (Keller & McKay, 1997; Noble et al., 2005). In addition, the amorphous rim without npFe of anorthosite implies possibly a micrometeorite impactor with iron-poor minerals. As described in the analysis in section 3, a large amount of npFeNi is formed in the vapor-deposited layer of minerals near kamacite. Therefore, the amorphous rim without npFe in 78221 may be still formed by iron-poor micrometeorite bombardment, although the rims show chemical evidence for preferential sputtering of constituent cations and are an erosional feature of solar wind implantation (Keller & McKay, 1997; Noble et al., 2005).

5. Conclusions

Micrometeorite bombardment of the surfaces of planetary bodies without the protection of atmosphere is a common phenomenon that changes the physical and chemical properties of soils exposed on the airless lunar surface. The differences of mineral compositions of the rocks determine the shapes and sizes of their laser pits. On the surfaces of olivine, pyroxene, and plagioclase, there are many silicate and aluminosilicate melt and vapor deposits. Furthermore, npFe or Fe-Ni alloy particles, with sizes ranging from several nanometers to hundreds of nanometers, are distributed on the surfaces of ilmenite, kamacite, and other minerals near kamacite.

The mineral subsurfaces of laser pits in basalt form a three-layer structure, including a completely amorphous layer, a partially amorphous layer, and a substrate. Because the melting points of pyroxene and ilmenite are lower than those of olivine and plagioclase, their partially amorphous layers are thinner than the completely amorphous layers in pyroxene and ilmenite and in olivine and plagioclase; the two amorphous layers have the same thickness. Due to the presence of a smaller temperature gradient and enough crystallization time in the partially amorphous layer, the npFe are mainly concentrated in this layer. Due to their higher contents of Fe, there are more npFe in olivine and pyroxene and fewer of them in plagioclase. In ilmenite, large iron inclusions are formed in the amorphous layer because there is a longer crystallization time caused by the lower melting point of ilmenite. The subsurface structure of kamacite in Huaxi ordinary chondrite includes a substrate and an amorphous layer with a large amount of npFe or Fe-Ni alloy inclusions. Silicate minerals of laser pits in Huaxi ordinary chondrite have outermost vapor-deposited layers containing many npFe that come from kamacite.

These differences in impact characteristics are expected to help determine the source material of npFe and infer the type of micrometeorite impactors bombarding the lunar soils. During micrometeorite bombardment, the npFe in the mare regions is likely produced simultaneously from lunar basalt and micrometeorites with iron-rich minerals, while the npFe in the highlands regions mainly come from micrometeorites.

References

- Bernatowicz, T. J., Nichols, R. H., Hohenberg, C. M., & Maurette, M. (1994). Vapor deposits in the lunar regolith. *Science*, 264(5166), 1779–1780. <https://doi.org/10.1126/science.264.5166.1779-a>
- Bibring, J. P., Maurette, M., Duraud, J. P., Durrieu, L., Meunier, R., & Jouret, C. (1972). Ultrathin amorphous coatings on lunar dust grains. *Science*, 175(4023), 753–755. <https://doi.org/10.1126/science.175.4023.753>
- Bradley, J. P. (1994). Chemically anomalous, preaccretionally irradiated grains in interplanetary dust from comets. *Science*, 265(5174), 925–929. <https://doi.org/10.1126/science.265.5174.925>
- Brunetto, R., Romano, F., Blanco, A., Fonti, S., Martino, M., Orofino, V., & Verrienti, C. (2006). Space weathering of silicates simulated by nanosecond pulse UV excimer laser. *Icarus*, 180(2), 546–554. <https://doi.org/10.1016/j.icarus.2005.10.016>
- Chapman, C. R. (2004). Space weathering of asteroid surfaces. *Annual Review of Earth and Planetary Sciences*, 32, 539–567. <https://doi.org/10.1146/annurev.earth.32.101802.120453>

Acknowledgments

This study was supported by the Knowledge Innovation Program of the Chinese Academy of Sciences (Lunar Program of Geochemical Institute), Youth Innovation Promotion Association of CAS (2014359) and the National Natural Science Foundation of China (General Program 41373067, 41403057, and Major Program 41490630). We thank the two reviewers who enhanced this document via their comments and editorial suggestions. The data for all figures and supporting information in this paper have been done by Yanxue Wu (Institute of Geochemistry Chinese Academy of Sciences). The data of melting points and densities in Table 1 are freely available at <https://www.americanelements.com/>.

- Christoffersen, R., Mckay, D. S., & Keller, L. P. (1994). Grain rims on ilmenite in the lunar regolith: Comparison to vapor deposits on regolith silicates, paper presented at Lunar and Planetary Science Conference.
- Christoffersen, R., Mckay, D. S., & Keller, L. P. (1996). Microstructure, chemistry, and origin of grain rims on ilmenite from the lunar soil finest fraction. *Meteoritics and Planetary Science*, 31(6), 835–848.
- Christoffersen, R., Loeffler, M. J., Dukes, C. A., Keller, L. P., & Baragiola, R. A. (2016). Compositional and microstructural evolution of olivine under multiple-cycle pulsed laser irradiation as revealed by FIB/Field-emission TEM, in *47th Lunar and Planetary Science Conference*, edited, p. Abstract #2747, Lunar and Planetary Institute, Houston.
- Clark, B., Hapke, B., Pieters, C., & Britt, D. (2002). Asteroid space weathering and regolith evolution. *Asteroids III*, 585–589.
- Dobrica, E., & Oglione, R. C. (2016). Adhering grains and surface features on two Itokawa particles. *Earth, Planets and Space*, 68. <https://doi.org/10.1186/s40623-016-0391-7>
- Fassett, C. I., & Minton, D. A. (2013). Impact bombardment of the terrestrial planets and the early history of the Solar System. *Nature Geoscience*, 6(7), 520–524. <https://doi.org/10.1038/ngeo1841>
- Gillis-Davis, J. J., Lucey, P. G., Bradley, J. P., Ishii, H. A., Kaluna, H. M., Misra, A., & Connolly, H. C. Jr. (2017). Incremental laser space weathering of Allende reveals non-lunar like space weathering effects. *Icarus*, 286, 1–14. <https://doi.org/10.1016/j.icarus.2016.12.031>
- Grant, R. W., Housley, R. M., & Paton, N. E. (1973). Origin and characteristics of excess Fe metal in lunar glass welded aggregates.
- Hapke, B. (2001). Space weathering from Mercury to the asteroid belt. *Journal of Geophysical Research*, 106(E5), 10,039–10,073. <https://doi.org/10.1029/2000JE001338>
- Hapke, B., Cassidy, W., & Wells, E. (1975). Effects of vapor-phase deposition processes on optical, chemical, and magnetic-properties of lunar regolith. *Moon*, 13(1–3), 339–353. <https://doi.org/10.1007/bf00567525>
- Keller, L. P., & McKay, D. S. (1993). Discovery of vapor deposits in the lunar regolith. *Science*, 261(5126), 1305–1307. <https://doi.org/10.1126/science.261.5126.1305>
- Keller, L. P., & McKay, D. S. (1997). The nature and origin of rims on lunar soil grains. *Geochimica et Cosmochimica Acta*, 61(11), 2331–2341. [https://doi.org/10.1016/s0016-7037\(97\)00085-9](https://doi.org/10.1016/s0016-7037(97)00085-9)
- Kissel, J., & Krueger, F. R. (1987). Ion formation by impact of fast dust particles and comparison with related techniques. *Applied Physics A: Materials Science & Processing*, 42(1), 69–85. <https://doi.org/10.1007/bf00618161>
- Li, Y., Li, X. Y., Wang, S. J., Li, S. J., Tang, H., & Coulson, I. M. (2013). Crystal orientation results in different amorphization of olivine during solar wind implantation. *Journal of Geophysical Research, Planets*, 118, 1974–1982. <https://doi.org/10.1002/Jgre.20151>
- Loeffler, M. J., Baragiola, R. A., & Murayama, M. (2008). Laboratory simulations of redeposition of impact ejecta on mineral surfaces. *Icarus*, 196(1), 285–292. <https://doi.org/10.1016/j.icarus.2008.02.021>
- Loeffler, M. J., Dukes, C. A., Christoffersen, R., & Baragiola, R. A. (2016). Space weathering of silicates simulated by successive laser irradiation: In situ reflectance measurements of Fo(90), Fo(99+), and SiO₂. *Meteoritics and Planetary Science*, 51(2), 261–275. <https://doi.org/10.1111/maps.12581>
- Matsuoka, M., Nakamura, T., Kimura, Y., Hiroi, T., Nakamura, R., Okumura, S., & Sasaki, S. (2015). Pulse-laser irradiation experiments of Murchison CM2 chondrite for reproducing space weathering on C-type asteroids. *Icarus*, 254, 135–143. <https://doi.org/10.1016/j.icarus.2015.02.029>
- Moroz, L. V., Fisenko, A. V., Semjonova, L. F., Pieters, C. M., & Korotaeva, N. N. (1996). Optical effects of regolith processes on S-asteroids as simulated by laser shots on ordinary chondrite and other mafic materials. *Icarus*, 122(2), 366–382. <https://doi.org/10.1006/icar.1996.0130>
- Morris, R. V. (1980). Origins and size distribution of metallic iron particles in the lunar regolith.
- Noble, S. K., Keller, L. P., & Pieters, C. M. (2005). Evidence of space weathering in regolith breccias I: Lunar regolith breccias. *Meteoritics and Planetary Science*, 40(3), 397–408.
- Noble, S. K., Keller, L. P., & Pieters, C. M. (2010). Evidence of space weathering in regolith breccias II: Asteroidal regolith breccias. *Meteoritics and Planetary Science*, 45(12), 2007–2015. <https://doi.org/10.1111/j.1945-5100.2010.01151.x>
- Noble, S. K., Hiroi, T., Keller, L. P., Rahman, Z., Sasaki, S., & Pieters, C. M. (2011). Experimental space weathering of ordinary chondrites by nanopulse laser: TEM results, *Noble S K*.
- Noble, S. K., Keller, L. P., Christoffersen, R., & Rahman, Z. (2016). The microstructure of lunar micrometeorite impact craters, in *47th Lunar and Planetary Science Conference*, edited, p. Abstract #1465, Lunar and Planetary Institute, Houston.
- Noguchi, T., Kimura, M., Hashimoto, T., Konno, M., Nakamura, T., Zolensky, M. E., ... Ishibashi, Y. (2014). Space weathered rims found on the surfaces of the Itokawa dust particles. *Meteoritics and Planetary Science*, 49(2), 188–214. <https://doi.org/10.1111/maps.12111>
- Pieters, C. M., & Noble, S. K. (2016). Space weathering on airless bodies. *Journal of Geophysical Research, Planets*, 121, 1865–1884. <https://doi.org/10.1002/2016JE005128>
- Pieters, C. M., Taylor, L. A., Noble, S. K., Keller, L. P., Hapke, B., Morris, R. V., ... Wentworth, S. (2000). Space weathering on airless bodies: Resolving a mystery with lunar samples. *Meteoritics and Planetary Science*, 35(5), 1101–1107.
- Sasaki, S., Nakamura, K., Hamabe, Y., Kurahashi, E., & Hiroi, T. (2001). Production of iron nanoparticles by laser irradiation in a simulation of lunar-like space weathering. *Nature*, 410(6828), 555–557. <https://doi.org/10.1038/35069013>
- Sasaki, S., Hiroi, I., Nakamura, K., Hamabe, Y., Kurahashi, E., & Yamada, M. (2002). Simulation of space weathering by nanosecond pulse laser heating: Dependence on mineral composition, weathering trend of asteroids and discovery of nanophase iron particles. In J. Klinger, & D. Mohlmann (Eds.), *Modelling and laboratory studies supporting space missions to small bodies* (pp. 783–788). Oxford: Pergamon-Elsevier Science Ltd. [https://doi.org/10.1016/s0273-1177\(02\)00012-1](https://doi.org/10.1016/s0273-1177(02)00012-1)
- Taylor, L. A., Pieters, C. M., Keller, L. P., Morris, R. V., & McKay, D. S. (2001). Lunar mare soils: Space weathering and the major effects of surface-correlated nanophase Fe. *Journal of Geophysical Research*, 106(E11), 27,985–27,999. <https://doi.org/10.1029/2000JE001402>
- Thompson, M. S., Christoffersen, R., Zega, T. J., & Keller, L. P. (2014). Microchemical and structural evidence for space weathering in soils from asteroid Itokawa. *Earth, Planets and Space*, 66, 10. <https://doi.org/10.1186/1880-5981-66-89>
- Thompson, M. S., Zega, T. J., Keane, J. T., Becerra, P., & Byrne, S. (2015). The oxidation state of Fe nanoparticles in lunar soil: Implications for space weathering processes, *46th Lunar and Planetary Science Conference (2015)*, 2932.
- Thompson, M. S., Zega, T. J., Becerra, P., Keane, J. T., & Byrne, S. (2016). The oxidation state of nanophase Fe particles in lunar soil: Implications for space weathering. *Meteoritics and Planetary Science*, 51(6), 1082–1095. <https://doi.org/10.1111/maps.12646>
- Wasson, J. T., Pieters, C. M., Fisenko, A. V., Semjonova, L. F., & Warren, P. H. (1998). Simulation of space weathering of eucrites by laser impulse irradiation, *29th Annual Lunar and Planetary Science Conference*, pp. 1940.
- Yamada, M., Sasaki, S., Nagahara, H., Fujiwara, A., Hasegawa, S., Yano, H., ... Otake, H. (1999). Simulation of space weathering of planet-forming materials: Nanosecond pulse laser irradiation and proton implantation on olivine and pyroxene samples. *Earth, Planets and Space*, 51(11), 1255–1265.